

Atomic Structure and Dynamics of Defects in 2D MoS₂ Bilayers

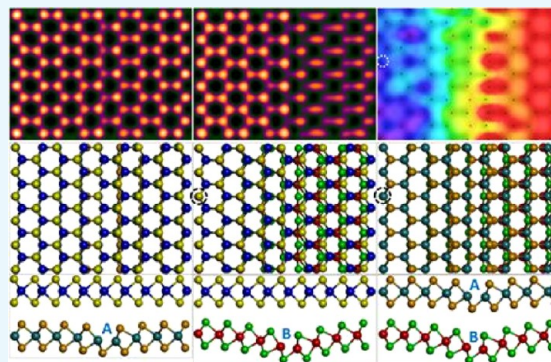
Si Zhou,[†] Shanshan Wang,^{†,ID} Huashan Li,[‡] Wenshuo Xu,[†] Chuncheng Gong,[†] Jeffrey C. Grossman,[‡] and Jamie H. Warner^{*,†,ID}

[†]Department of Materials, University of Oxford, 16 Parks Road, Oxford OX1 3PH, U.K.

[‡]Department of Materials Science and Engineering, Massachusetts Institute of Technology, 77 Massachusetts Avenue, Cambridge, Massachusetts 02139, United States

Supporting Information

ABSTRACT: We present a detailed atomic-level study of defects in bilayer MoS₂ using aberration-corrected transmission electron microscopy at an 80 kV accelerating voltage. Sulfur vacancies are found in both the top and bottom layers in 2H- and 3R-stacked MoS₂ bilayers. In 3R-stacked bilayers, sulfur vacancies can migrate between layers but more preferably reside in the (Mo–2S) column rather than the (2S) column, indicating more complex vacancy production and migration in the bilayer system. As the point vacancy number increases, aggregation into larger defect structures occurs, and this impacts the interlayer stacking. Competition between compression in one layer from the loss of S atoms and the van der Waals interlayer force causes much less structural deformations than those in the monolayer system. Sulfur vacancy lines neighboring in top and bottom layers introduce less strain compared to those staggered in the same layer. These results show how defect structures in multilayered two-dimensional materials differ from their monolayer form.



INTRODUCTION

Transition metal dichalcogenides (TMDs), such as MoS₂ and WS₂, are direct band gap semiconductors in their monolayer form and indirect band gap semiconductors in bulk.^{1–4} They offer band gaps in the red visible spectrum and semiconducting properties that expand the application of two-dimensional (2D) materials beyond what graphene alone can achieve.^{5–7} The presence of defects in TMDs influences the photoluminescence spectra, electron transport behavior, and photosensing capabilities.^{8–12} Understanding the structure of the defects is important for developing an accurate picture of their impact on properties. Aberration-corrected transmission electron microscopy (AC-TEM) is one of the leading approaches to study the atomic structure of defects in 2D materials.¹³

With the availability of monolayer TMDs, detailed atomic-level studies of vacancies in MoS₂ and other S- and Se-based TMDs have been performed.^{14–24} However, no detailed studies on the structure and dynamics of defects in bilayer TMDs have been reported. MoS₂ or WS₂ bilayers have two natural stacking forms: 3R and 2H stacking, with 2H dominating due to energetic preference.^{25,26} Most recent work has been focused on the 2H stacking structure and related optical properties²⁷ and some has been performed on 3R-stacked MoS₂ due to its relative rarity.²⁸

Upon 80 kV electron beam irradiation of MoS₂ and WS₂, S vacancies are created and also mobilized, resulting in point defects that combine to form line defects.^{14,29–32} The line defects in MoS₂ can extend in length and also in width. As the

length of a one sulfur vacancy line (1SVL) defect increases, large lattice compression occurs to accommodate the loss of S atoms and change in charge density around the Mo atoms. This also causes large out-of-plane distortion to the monolayer sheet, similar to the buckling in graphene monolayers caused by dislocations.³³ The ability of monolayer sheets to buckle when defects are introduced plays an important role in strain relief.³⁴ Recent work has shown that heating graphene to high temperatures causes the substrate it is attached to expand and produce tension on graphene.³⁵ This in turn causes partial dislocations to occur because single dislocation cores are only stable when accompanied by out-of-plane buckling. The ability of a 2D material to accommodate buckling and defects is expected to be different as more layers are added, due to the interlayer van der Waals forces. Unique interlayer interactions have been previously seen in bilayer graphene, with very small mismatch angles between the layers, causing local regions of commensurate and incommensurate stacking.³⁶ Recent work has shown that as the width of line vacancies in MoS₂ increases, the rows of S vacancy lines are staggered from top to bottom to enable stable bond restructuring.¹² The reconstructed bonds have different unit cell structures, and this will cause changes in the local van der Waals interactions with the second layer in bilayer 2D systems. Furthermore, the compression associated

Received: June 6, 2017

Accepted: June 20, 2017

Published: July 7, 2017

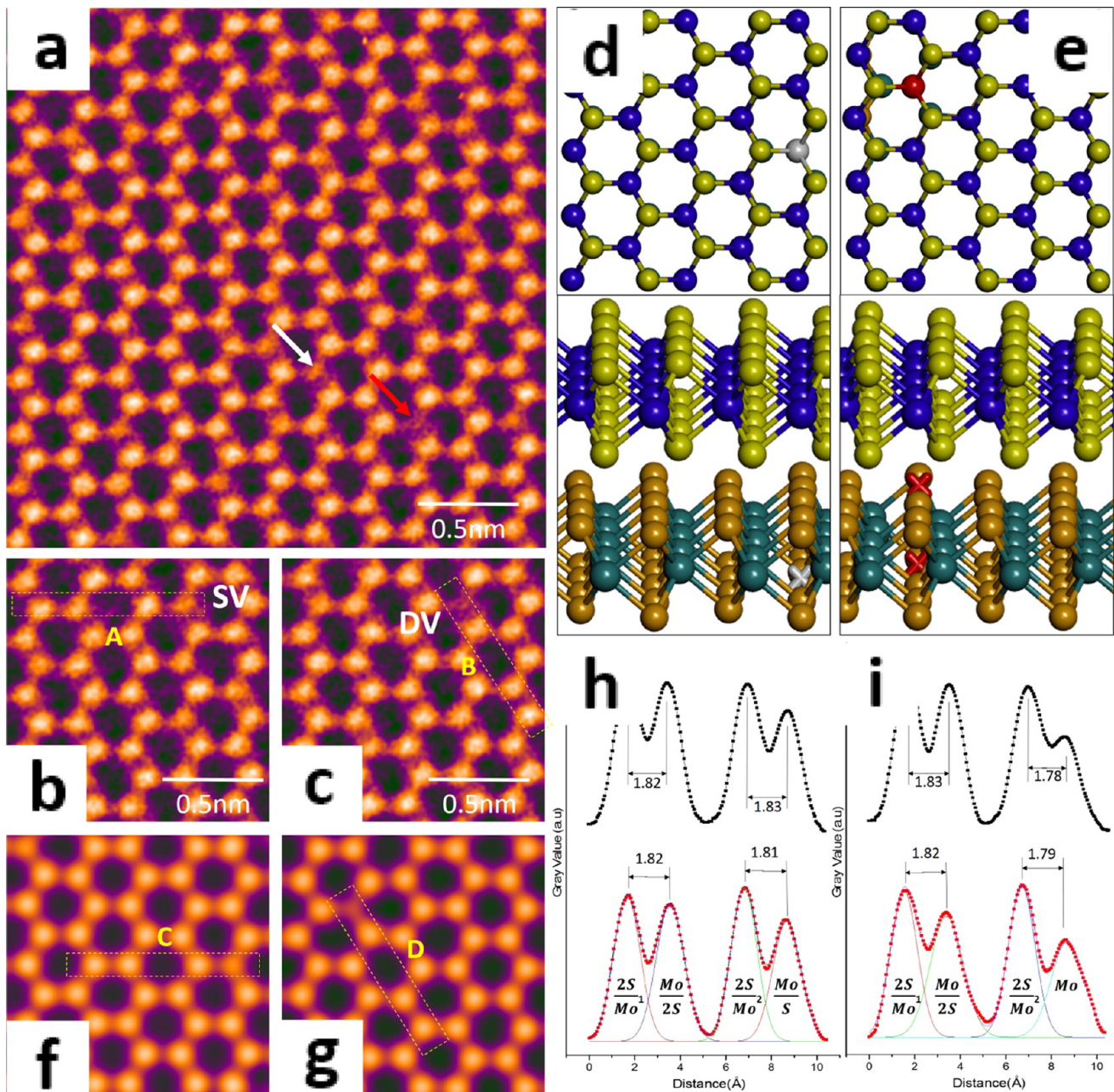


Figure 1. (a) AC-TEM image of SVs and DVs in 2H-stacked bilayer MoS₂, marked by white and red arrows, respectively. Zoomed in high-resolution transmission electron microscopy (HRTEM) image indicating (b) SVs and (c) DVs. (f, g) Multislice image simulations based on DFT-calculated atomic models with (d) one missing S atom and (e) two missing S atoms in the Mo–S–S column, respectively. The color key is SV = gray, DV = red. (h) Boxed line profiles of the SVs shown in (b) and (f). (i) Boxed line profiles of the DVs shown in (c) and (g).

with the multiple stacked line vacancies in MoS₂ will cause local shifts in atomic positions extending out from the defect region, and this will give rise to competition between in-plane compression around defects and interlayer van der Waals forces and associated 2H and 3R stacking phases.

In this study, MoS₂ samples are grown on Si substrates with a 300 nm oxide layer using methods based on our prior work.¹² Samples of MoS₂ are predominantly monolayers, but sometimes, small bilayer domains are found. We study the structure and dynamics of defects in bilayer MoS₂, from point defects to aggregated clusters. Both 2H- and 3R-stacked bilayers are examined due to their presence in chemical vapor deposition (CVD)-grown samples. Density functional theory (DFT)

calculations are used to provide accurate model structures for multislice image simulations to compare to the experimental phase contrast AC-TEM images.

RESULTS AND DISCUSSION

For our as-grown monolayer and few-layer MoS₂ (as indicated in Figure S1), the interface of the monolayer and 2H-stacked bilayer MoS₂ are shown in Figure S2a,b. First, we examine the presence of S vacancies in the 2H-stacked bilayer MoS₂ (Figure 1). Electron beam irradiation at 80 kV is known to introduce sulfur vacancies in MoS₂.¹³ Figure 1a shows a typical AC-TEM image of a 2H-stacked bilayer, with visible weaker contrast spots marked by white and red arrows. The magnified images in

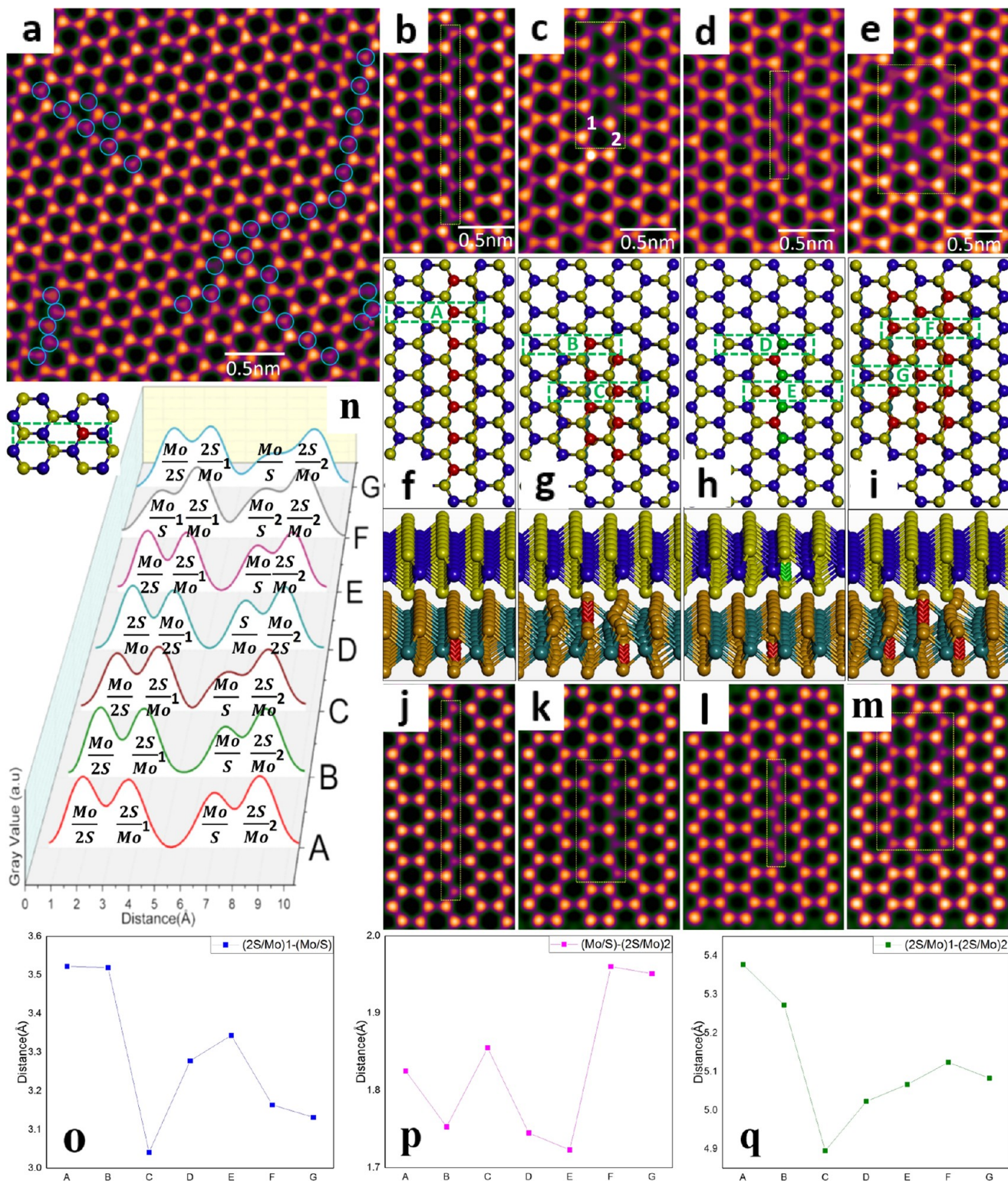


Figure 1b,c show two different levels of reduced contrast associated with single S vacancies (SVs) and double S vacancies (DVs) in the same column. Atomic models of 1SV (gray) and 1DV (red) from DFT calculations are respectively shown in **Figure 1d,e** in both top (colored ball) and three-dimensional (3D) views (colored cross). Corresponding multislice image

Figure 1b,c show two different levels of reduced contrast associated with single S vacancies (SVs) and double S vacancies (DVs) in the same column. Atomic models of 1SV (gray) and 1DV (red) from DFT calculations are respectively shown in **Figure 1d,e** in both top (colored ball) and three-dimensional (3D) views (colored cross). Corresponding multislice image

1DV (red) from DFT calculations are respectively shown in **Figure 1d,e** in both top (colored ball) and three-dimensional (3D) views (colored cross). Corresponding multislice image

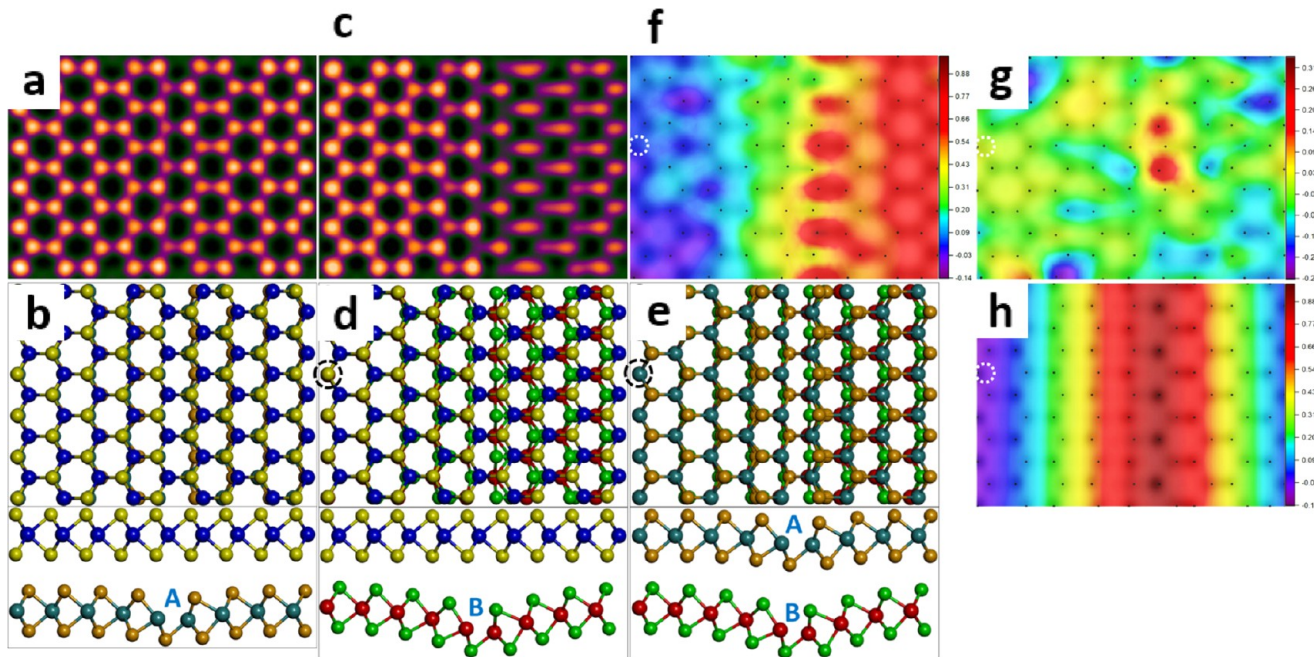


Figure 3. Multislice image simulations of (a) bilayer MoS₂ with 1SVL in layer A and (c) one pristine monolayer on top of one defective layer B and (b, d) corresponding DFT-calculated atomic models. (e) Atomic model of “bilayer” composed by layers A and B. Two-dimensional displacement maps along (f) *x*, (g) *y*, and (h) *z* directions, respectively, which are laid on top of a simulated image based on (e). Alignment points are marked with black circles in the image simulations, and reference points are marked with white circles in displacement maps.

simulations (Figure 1f,g) and line profile analysis (Figure 1h,i) show good similarity with the experimental results, confirming SVs and DVs in 2H-stacked bilayer MoS₂.

Under prolonged electron beam irradiation, SVs and DVs in 2H bilayer MoS₂ increase in density and start to aggregate into extended line defects, as shown in Figure 2a. The line defects in 2H bilayer MoS₂ can exist in variable lengths along the zigzag directions and also gain width along the armchair direction (Figure 2b–e). The magnified AC-TEM image in Figure 2b shows a 1SVL, with a length of 7SVs. The corresponding DFT-calculated model, in top and 3D views (Figure 2f), shows negligible in-plane or out-of-plane lattice distortions, triggered by losing seven S atoms in the bottom layer, which differs from the findings of prior studies on 1SVLs in monolayer MoS₂.¹³ Two types of 2SVLs are observed (Figure 2c,d), with different S reconstructions. Two corresponding DFT-calculated models are evaluated (Figure 2g,h). Type A has 2SVLs within only one MoS₂ layer, with alternate staggering across top and bottom S sites. On the basis of a previous report,¹² the staggering configuration of two vacancy lines in the bottom layer is energetically preferred. Type B has one 1SVL in the bottom and the other in the top MoS₂ layer, giving a 2SVL defect overall, spread across the two layers. The vacancy lines can exist in either plane of each layer. DFT calculations indicate that no obvious out-of-plane distortion occurs in either type A or B 2SVLs in the 2H bilayer, which is different from that in the 2SVL in monolayer MoS₂. The observation of type B 2SVL also indicates the coexistence of S vacancies in both the bottom and top layers in the 2H-stacked MoS₂ bilayer. In Figure 2e, a 3SVL is presented, showing a similar structure to that of A-2SVL. The atomic model relaxed using DFT calculations (Figure 2i) shows a staggered arrangement of SVLs in the bottom layer.

To quantify the lattice distortion introduced by each SVL in 2H bilayer MoS₂ (Figure 2n), we measured the boxed line profiles across (Mo/2S)–(2S/Mo)₁–(Mo/S)–(2S/Mo)₂ col-

umns, as marked by green dashed rectangles for 1SVL (A), A-2SVL (B and C), B-2SVL (D and E), and 3SVL (F and G). The distance between each column is determined by fitting Gaussian curves and plotted for A–G in Figure 2o–q. For 1SVL, the (2S/Mo)₁–(Mo/S), (Mo/S)–(2S/Mo)₂, and (2S/Mo)₁–(2S/Mo)₂ distances are 3.52, 1.83, and 5.38 Å, respectively. The negligible shrinkage compared to the column distances in pristine 2H bilayer MoS₂ confirms minimal compression in the system when losing seven S atoms in a layer. The line profiles along directions B and C, the left-side SVL in A-2SVL, show no (2S/Mo)₁–(Mo/S) distance change but a slight drop in the (Mo/S)–(2S/Mo)₂ and (2S/Mo)₁–(2S/Mo)₂ distances. However, for the right-side SVL, the (2S/Mo)₁–(Mo/S) and (2S/Mo)₁–(2S/Mo)₂ distances shrink to 3.04 and 4.90 Å, with a small increase in the (2S/Mo)₁–(Mo/S) distance. These changes indicate greater compression introduced between the two staggered SVLs. For the right-side SVL, the (2S/Mo)₁–(Mo/S) distance increment, indicating tension, is caused by the displacement of S atoms in (Mo/S) toward the (2S/Mo) column. The directions D and E in B-2SVL both show compression along the armchair direction. Compared to those in A-2SVL, no tension exists in the defective regions and the contraction is relatively smaller, indicating that the configuration having one sulfur vacancy line in each layer introduces less strain into the bilayer system. The staggered 3SVL shows expansion of the (Mo/S)–(2S/Mo)₂ distance and shrinkage of the (2S/Mo)₁–(2S/Mo)₂ distance, as expected.

Figure 3a shows a multislice image simulation of 2H-stacked bilayer MoS₂ with an infinitely long 1SVL running through the bottom layer on the DFT-calculated atomic model in Figure 3b. As discussed before, the introduction of 1SVL introduces negligible out-of-plane and in-plane lattice distortions. To compare the difference between the SVLs in the monolayer and bilayer system, as shown in Figure 3d, layer B is DFT-calculated

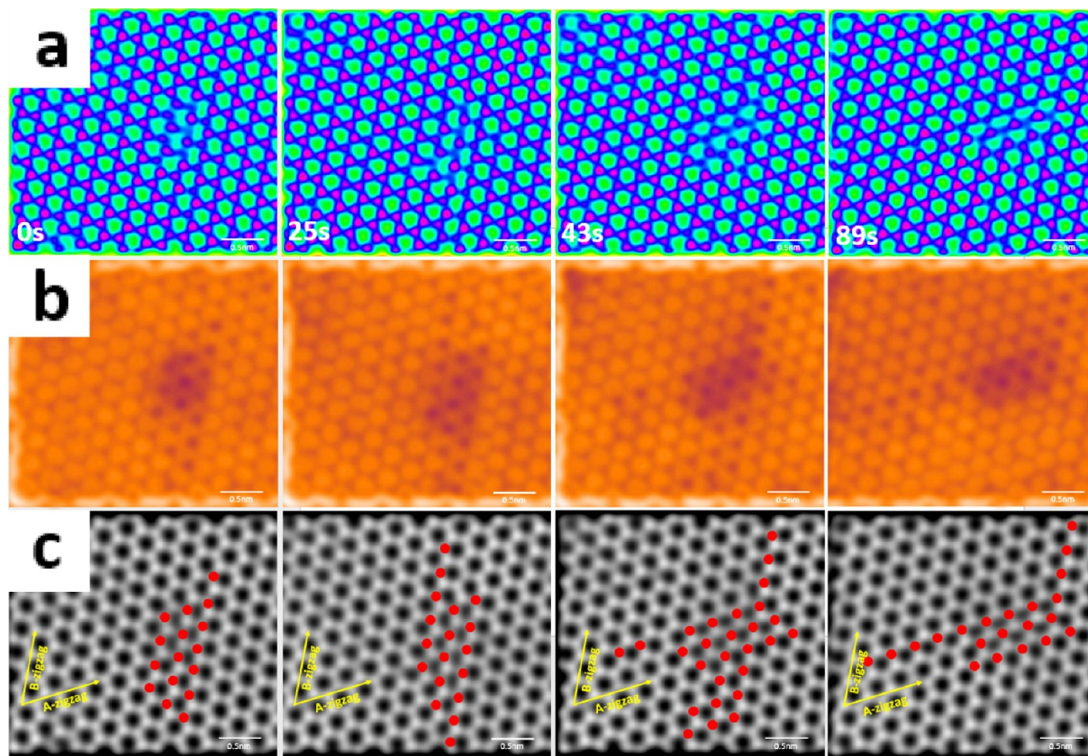


Figure 4. (a) Series of processed AC-TEM images showing the evolution of S vacancies in 2H bilayer MoS₂ over 89 s (a false color LUT is used to highlight vacancies). (b) S vacancies highlighted as darker spots using different false color LUTs. (c) Gray scale image showing vacancy migration and 3SVL rotation from the B-zigzag to the A-zigzag direction (S vacancies are marked as red dots).

model for monolayer MoS₂ with 1SVL running through, another pristine MoS₂ monolayer is manually placed on top to create similar 2H stacking configuration, taking the circled column as the alignment point. The corresponding multislice image simulation in Figure 3c shows considerable lattice distortion on the right-hand side of the 1SVL, resulting from the mismatch between two layers. Layers A and B are then extracted and stacked, as shown in Figure 3e; the column circled in black is chosen as the alignment point. From the side view, a large discrepancy in the out-of-plane distortion between layers A and B can be distinguished. To quantify the lattice mismatch in the system, 2D displacement maps from the *x*, *y*, and *z* axes are constructed in Figure 3f–h, respectively. The reference point is circled in white. The displacement maps show significant compression with increased magnitude in the *x* direction. However, the lattice mismatch in the *y* direction is uniformly distributed and relatively small. The displacement map in the *Z* axis shows a centrosymmetric configuration, with most significant *Z*-direction distortion in the defective site and lowest, in the reference point, further confirming a large out-of-plane distortion difference between the two layers. We further measure the bond length of Mo–S in the defective site (shown in Figure S5). Compared to the value of 2.41 in pristine MoS₂, the maximum bond length deviation for layers A and B is, respectively, 3.7 and 6.6%, indicating that the compression in the *x* direction also mainly comes from the out-of-plane distortion. Therefore, SVLs in the monolayer system introduce slightly larger in-plane lattice deformations than those in their bilayer counterparts. However, the main discrepancy between the defective layer in monolayer and bilayer systems is the out-of-plane distortion. The considerable buckling introduced by SVLs in monolayer MoS₂ becomes insignificant in bilayer

system, mainly compensated by the interlayer van der Waals force.

The sequential AC-TEM images in Figure 4a show the dynamics of S vacancies in 2H-stacked bilayer MoS₂ during 89 s of electron beam irradiation. A different false color look up table (LUT) is applied to highlight every SV in each frame (Figure 4b). In Figure 4c, the gray scale image with red dots indicating SVs shows that during the first 25 s the 3SVL gains length in the B-zigzag direction. Vacancies initially aggregate along the A-zigzag direction from 25 to 43 s. Over the latter 46 s, a large number of vacancies along the B-zigzag direction are quenched and the SVL transforms to 3SVL along the A-zigzag direction. In the first 43 s, newly ejected S atoms adjacent to the 3SVL are introduced under electron beam irradiation. In the next 46 s, vacancies along the B-zigzag direction get quenched by free S atoms or migrate in the A-zigzag direction.

A monolayer–3R-stacked bilayer interface has also been observed in our study (Figure S2c,d). Figure 5a shows a typical AC-TEM image of 3R-stacked bilayer MoS₂, in which a large number of bright spots (marked by white and purple arrows) and blurred regions (marked by green and red arrows) are observed. Magnified AC-TEM images in Figure 5b–e indicate SVs (SV₁ and SV₂) and DVs (DV₁ and DV₂) as blurred regions, bright spots, heavily blurred regions, and brighter spots, respectively. The existence of 3R-stacked bilayer MoS₂ is confirmed by imaging the structure under different defocus values, leading to contrast pattern variations that the 2H structure cannot exhibit. The corresponding multislice image simulations under different defocus values match the experimental results (Figure S4). Atomic models relaxed by DFT (Figure 5f–i) and their corresponding multislice image simulations (Figure 5j–m) indicate that the blurriness is due to losing one (SV₁) or two (DV₁) S atoms in a 2S/Mo column

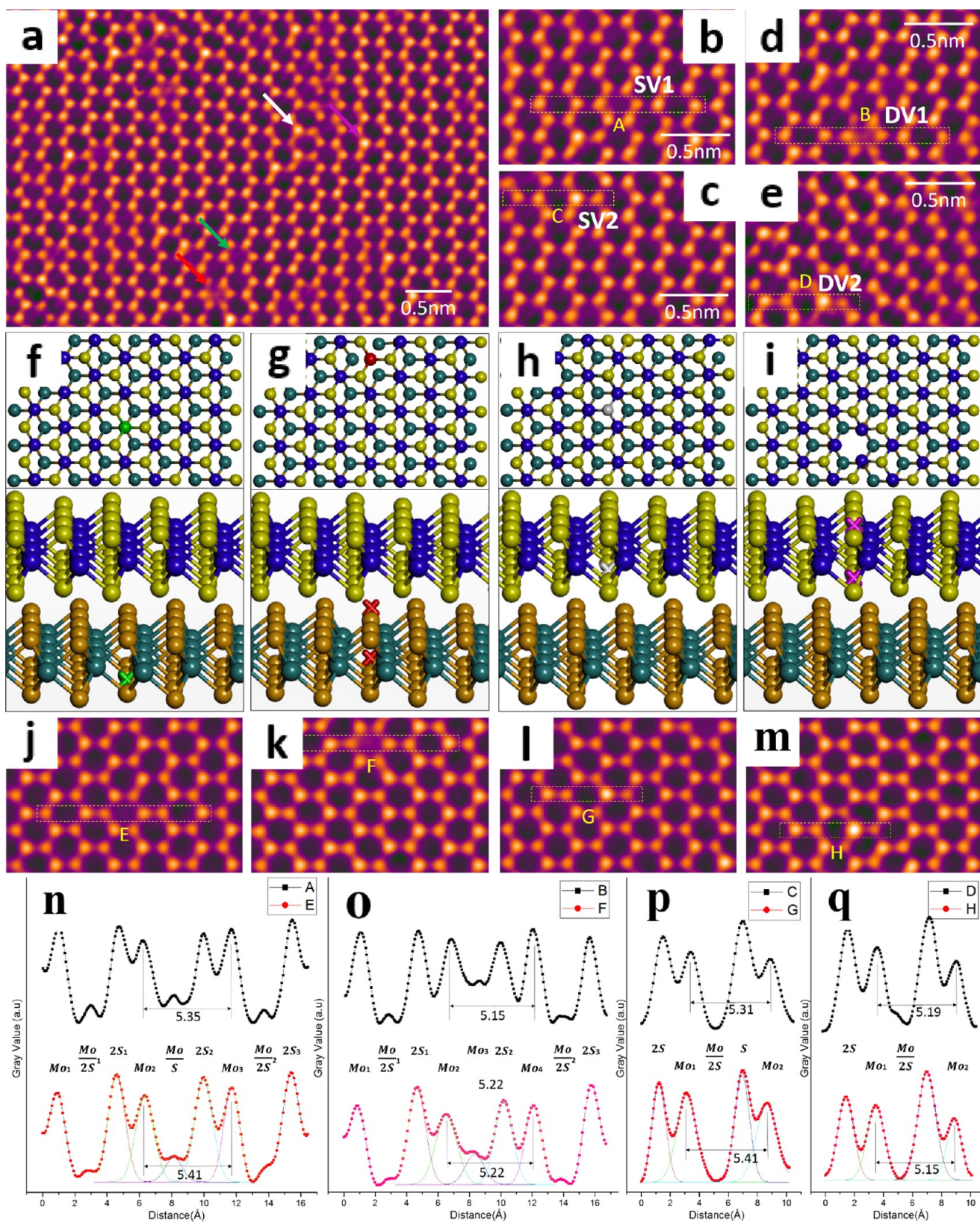


Figure 5. (a) AC-TEM image showing the distribution of S vacancies in 3R-stacked bilayer MoS₂. The color key is SV₁ = green, DV₁ = red, SV₂ = gray, DV₂ = purple. Zoomed in HRTEM image indicating (b) SV₁, (c) SV₂, (d) DV₁, and (e) DV₂. (j–m) Multislice image simulations based on DFT-calculated atomic models of a 3R-stacked MoS₂ bilayer with (f) one missing S atom and (g) two missing S atoms in the Mo-S-S column and (h) one missing S atom and (i) two missing S atoms in the S-S column, respectively. Vacancies are marked as colored balls in the top view and crosses in the 3D view. (n–q) Boxed line profiles taken along the yellow dashed rectangles marked A–H.

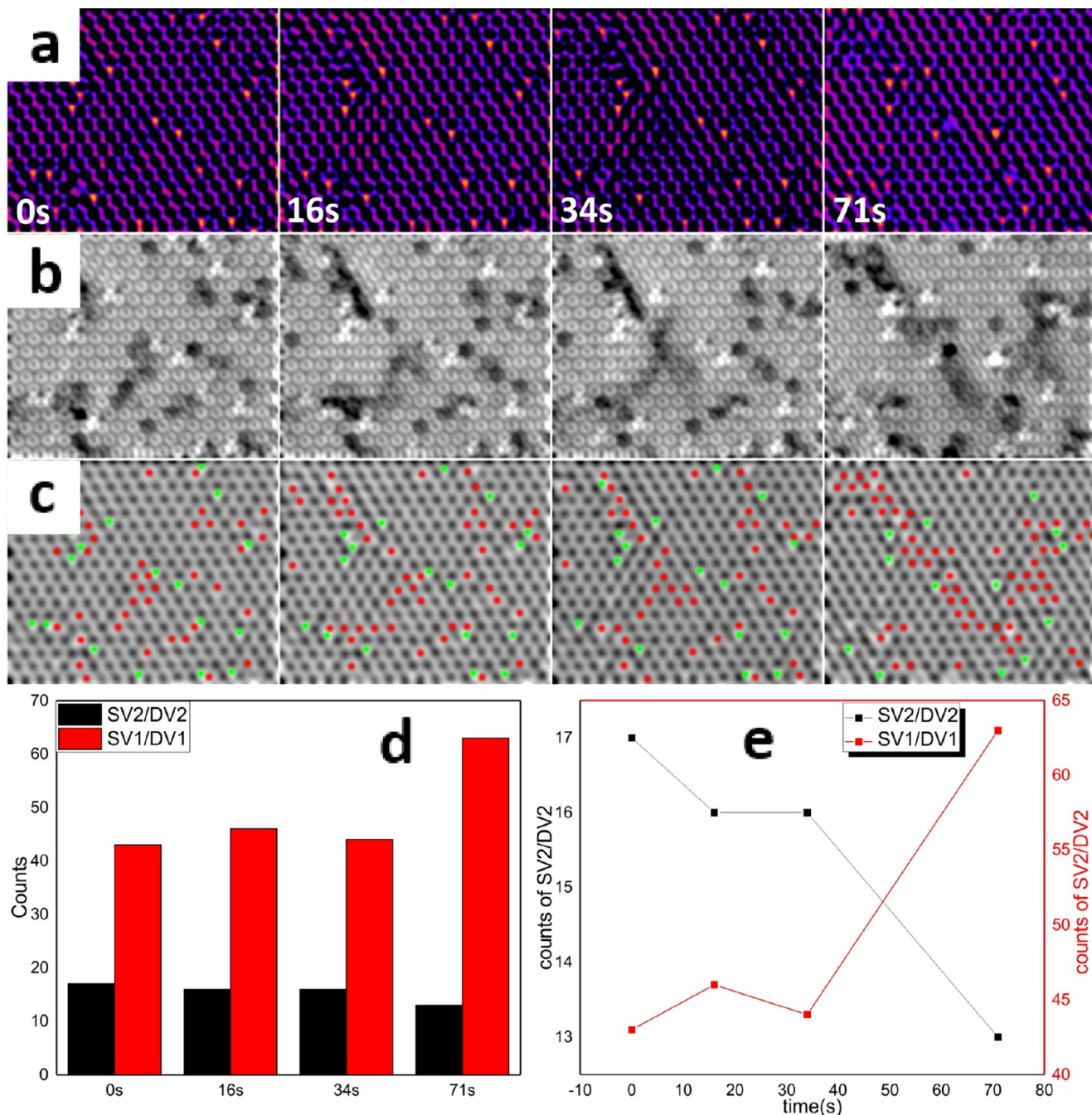


Figure 6. Processed AC-TEM images showing the evolution of (a) SV₂/DV₂ as bright spots and (b) SV₁/DV₁ as dimmed regions over 71 s. (c) Distribution of SV₁/DV₁ and SV₂/DV₂ marked as red and green spots, respectively. (d) Histogram and (e) trend lines representing the number change of SV₁/DV₁ and SV₂/DV₂ as a function of time.

and that the bright contrast is due to losing one (SV₂) or two (DV₂) S atoms in a 2S column. Intensity line profiles along the yellow arrows in both simulated and experimental images are taken covering the defective site. For both SVs (SV₁ and SV₂), the Mo–Mo column distance remains close to that in pristine 3R bilayer MoS₂ (5.4 Å), implying that nearly no compression is introduced to the bilayer by losing one S atom. In contrast, a column distance shrinkage of ~5% is observed for both DV₁ and DV₂, indicating small contraction caused by losing both S atoms in 2S or Mo/2S columns. These results are consistent with those on the SVs/DVs in 2H bilayer MoS₂. Further confirmation of the existence of SVs/DVs in 3R-stacked bilayer

MoS₂ is obtained by measuring the peak intensity ratio at multiple defective sites, as shown in Figures 5n–q and S3.

Processed AC-TEM images in Figure 6a,b highlight SV₂/DV₂ and SV₁/DV₁ as bright spots and dark regions, respectively. Figure 6c demonstrates the evolution of SV₂/DV₂ (green) and SV₁/DV₁ (red) under electron beam irradiation. The number of each SV is calculated as a function of time, as displayed in the histogram (Figure 6d) and plot (Figure 6e). Throughout the frames, the ratio of SV₁/DV₁ to SV₂/DV₂ increases from 2.5:1 to 4.9:1, indicating the dominance of SV₁/DV₁. Therefore, for 3R-stacked bilayer MoS₂, under 80 kV irradiation, the S atoms in the 2S columns are more stable and less likely to be sputtered compared to those in the Mo/2S columns. Over 71 s,

the SV_2/DV_2 number drops slightly, whereas the density of SV_1/DV_1 increases, especially in the last 37 s. Hence, the most newly produced SV_1/DV_1 are derived from the prolonged irradiation. However, vacancy migration also happen from SV_2/DV_2 to SV_1/DV_1 , implying vacancy migration between layers in 3R bilayer MoS₂.

CONCLUSIONS

AC-TEM imaging is conducted under an accelerating voltage of 80 kV, allowing production and aggregation of vacancies as well as atomic-level resolution of defective regions in bilayer MoS₂. DFT-calculated models prove the different production and migration mechanisms between sulfur vacancies in monolayer and bilayer systems. The combination of DFT calculations and dislocation maps reveal that the main discrepancy between defective monolayer and bilayer systems is the out-of-plane lattice distortions. The ability for the bilayer sheet to accommodate the buckling and compression caused by line defects can be assigned to the competition between compression in one layer from the loss of S atoms and the interlayer van der Waals force.

METHODS

MoS₂ CVD Synthesis and Transfer. The synthesis of MoS₂ was executed in two individually controlled quartz tube furnaces with only Ar flowing at atmospheric pressure using S powder (1 g of purum grade >99.5%) and MoO₃ powder. The MoO₃ precursor was initially loaded in a 1 cm diameter tube, which was in turn placed inside a larger diameter (1 in.) tube of the CVD furnace. This was to prevent cross-contamination of S and MoO₃ prior to MoS₂ formation on the target substrate, with the S kept separate in the larger diameter outer tube. Two furnaces were used to control the temperature of each precursor and the substrate, with heating temperatures of S at 180 °C, MoO₃ at 300 °C, and the substrate at 800 °C. Ar was used as a carrier gas. The S was left to vaporize for an initial 15 min before the temperature of the second furnace was increased to 800 °C at 40 °C min⁻¹ and left for 15 min under an Ar flow of 150 sccm. The Ar flow was then reduced to 10 sccm for 25 min, followed by a fast cooling process (sample removal). The S temperature was kept at 180 °C throughout.

The as-grown sample was first spin-coated with a poly-(methyl methacrylate) (PMMA) scaffold (8 wt % in anisole, 495k molecular weight) at 4700 rpm for 60 s and then cured at 150 °C for 15 min. The edge of the wafer was ground with a diamond file to expose the SiO₂/Si edges to the etchant solution. The underlying SiO₂/Si substrate was subsequently detached by floating the sample on a 15 M KOH (Sigma-Aldrich) solution in a water bath for 2 h at 40 °C. The suspended PMMA–MoS₂ film was thoroughly cleaned by transferring and floating onto fresh deionized water several times. For the TEM characterization, the PMMA–MoS₂ film was transferred onto a holey Quantifoil TEM grid and left to dry overnight in air. PMMA–MoS₂–Quantifoil was subsequently baked at 150 °C for 15 min to improve sample adhesion. The sample was eventually prepared by removing PMMA using an 8 h acetone solution bath.

Electron Microscopy. AC-TEM was performed at an accelerating voltage of 80 kV using Oxford's JEOL 2200MCO, with an imaging CEOS corrector. The beam current density under imaging conditions was $\sim 10^5$ e nm⁻² s⁻¹, with typical exposure times of 1–3 s.

Image Simulations and Processing. Multislice image simulations were conducted using JEMS software with an 80 kV accelerating voltage, 5 nm defocus spread, 3 nm (for 2H stacking) or 9 nm (for 3R stacking) defocus value, and 5 μm Cs. To match the AC-TEM image in Figure S2d, the simulation in Figure S2h was performed using 1.6 nm twofold astigmatism and 300 nm second-order coma (180°). The brightness and contrast of the simulated images were adjusted according to the intensity of the known columns in the experimental images, such as the (2S/Mo), (2S), and (S/Mo) columns.

ImageJ was used to process the AC-TEM images. A bandpass filter (between 100 and 1 pixels) and a Gaussian blur were carefully applied to minimize long-range uneven illumination without affecting the interpretation of the original image. Figure 4b was processed by an 8 pixel Gaussian blur, followed by a “find edge” filter, then another 8 pixel Gaussian blur, and then using an “orange hot”-colored LUT, and finally, the contrast and brightness were adjusted. In Figure 6a, bright SVs in bilayer 3R-stacked MoS₂ were processed by fast Fourier transform (FFT) band pass (100–1 pixels) and then a Gaussian blur of 12 pixels, followed by contrast adjustment. Dark S vacancies, as shown in Figure 6b, were processed by an FFT band pass filter (100–1 pixels), then a Gaussian blur of 8 pixels, followed by a find edge filter, and then another 6 pixel Gaussian blur, and then, the contrast was adjusted.

DFT Calculation. Standard ab initio simulations within the DFT were performed, using the Vienna ab initio simulation package (VASP v5.4),³⁷ to explore the atomic structures of 2D MoS₂ bilayers with various defects in the 2H and 3R stacking configurations. Plane-wave and projector-augmented-wave type pseudopotentials were adopted,³⁸ with kinetic-energy cutoffs of up to 300 eV and the generalized gradient approximation-Perdew–Burke–Ernzerhof exchange-correlation functional.³⁹ The DFT-D2 method of Grimme was implemented to account for the Van der Waals interactions,⁴⁰ with a 50 Å cutoff radius for pair interactions. To eliminate artificial interactions between periodic images, a 20 Å vacuum was constructed in the direction perpendicular to that of the sheets. The initial structures were generated on the basis of the TEM images and relaxed until all forces were smaller than 0.02 eV Å⁻¹. The Γ point was used for geometric optimization of S vacancies and finite line defects, whereas a Monkhorst–Pack *k*-point grid⁴¹ of 9 × 1 × 1 was employed in relaxation of infinite line defects.

ASSOCIATED CONTENT

Supporting Information

The Supporting Information is available free of charge on the ACS Publications website at DOI: [10.1021/acsomega.7b00734](https://doi.org/10.1021/acsomega.7b00734).

Optical and SEM images of monolayer and bilayer regions in MoS₂; AC-TEM images of monolayer–bilayer interfaces in 2H and 3R MoS₂ bilayers; additional images of S vacancies in 2H and 3R bilayer MoS₂; AC-TEM images of 3R-stacked MoS₂ under different focusing conditions; bond length measurements for defective monolayer and defective layer from the bilayer ([PDF](#))

AUTHOR INFORMATION

Corresponding Author

*E-mail: Jamie.warner@materials.ox.ac.uk. Phone: +44 1865273790.

ORCID

Shanshan Wang: [0000-0003-3750-6737](https://orcid.org/0000-0003-3750-6737)

Jamie H. Warner: 0000-0002-1271-2019

Notes

The authors declare no competing financial interest.

ACKNOWLEDGMENTS

J.H.W. is grateful for the support from the Royal Society. C.G. is grateful for the support from the Clarendon Fund.

REFERENCES

- (1) Gong, Y.; Lin, J.; Wang, X.; Shi, G.; Lei, S.; Lin, Z.; Zou, X.; Ye, G.; Vajtai, R.; Yakobson, B. I.; et al. Vertical and in-Plane Heterostructures from WS₂/MoS₂ Monolayers. *Nat. Mater.* **2014**, *13*, 1135–1142.
- (2) Plechinger, G.; Nagler, P.; Kraus, J.; Paradiso, N.; Strunk, C.; Schüller, C.; Korn, T. Identification of excitons, trions and biexcitons in single-layer WS₂. *Phys. Status Solidi RRL* **2015**, *9*, 457–461.
- (3) Withers, F.; Bointon, T. H.; Hudson, D. C.; Craciun, M. F.; Russo, S. Electron Transport of WS₂ Transistors in a Hexagonal Boron Nitride Dielectric Environment. *Sci. Rep.* **2014**, *4*, No. 4967.
- (4) Sorkin, V.; Pan, H.; Shi, H.; Quek, S. Y.; Zhang, Y. W. Nanoscale Transition Metal Dichalcogenides: Structures, Properties, and Applications. *Crit. Rev. Solid State Mater. Sci.* **2014**, *39*, 319–367.
- (5) Komsa, H.-P.; Kotakoski, J.; Kurasch, S.; Lehtinen, O.; Kaiser, U.; Krasheninnikov, A. V. Two-Dimensional Transition Metal Dichalcogenides under Electron Irradiation: Defect Production and Doping. *Phys. Rev. Lett.* **2012**, *109*, No. 035503.
- (6) Wang, Q. H.; Kalantar-Zadeh, K.; Kis, A.; Coleman, J. N.; Strano, M. S. Electronics and Optoelectronics of Two-Dimensional Transition Metal Dichalcogenides. *Nat. Nanotechnol.* **2012**, *7*, 699–712.
- (7) Ma, Y.; Dai, Y.; Guo, M.; Niu, C.; Lu, J.; Huang, B. Electronic and Magnetic Properties of Perfect, Vacancy-Doped, and Nonmetal Adsorbed MoS₂, MoTe₂ and WS₂ Monolayers. *Phys. Chem. Chem. Phys.* **2011**, *13*, 15546–15553.
- (8) K C, S.; Longo, R. C.; Addou, R.; Wallace, R. M.; Cho, K. Impact of Intrinsic Atomic Defects on the Electronic Structure of MoS₂ Monolayers. *Nanotechnology* **2014**, *25*, No. 375703.
- (9) Lin, Y.-C.; Björkman, T.; Komsa, H.-P.; Teng, P.-Y.; Yeh, C.-H.; Huang, F.-S.; Lin, K.-H.; Jadczak, J.; Huang, Y.-S.; Chiu, P.-W.; et al. Three-Fold Rotational Defects in Two-Dimensional Transition Metal Dichalcogenides. *Nat. Commun.* **2015**, *6*, No. 6736.
- (10) Zhou, W.; Zou, X.; Najmaei, S.; Liu, Z.; Shi, Y.; Kong, J.; Lou, J.; Ajayan, P. M.; Yakobson, B. I.; Idrobo, J. C. Intrinsic Structural Defects in Monolayer Molybdenum Disulfide. *Nano Lett.* **2013**, *13*, 2615–2622.
- (11) Han, Y.; Hu, T.; Li, R.; Zhou, J.; Dong, J. Stabilities and Electronic Properties of Monolayer MoS₂ with One or Two Sulfur Line Vacancy Defects. *Phys. Chem. Chem. Phys.* **2015**, *17*, 3813–3819.
- (12) Wang, S.; Lee, G.-D.; Lee, S.; Yoon, E.; Warner, J. H. Detailed Atomic Reconstruction of Extended Line Defects in Monolayer MoS₂. *ACS Nano* **2016**, *10*, 5419–5430.
- (13) Hong, J.; Hu, Z.; Probert, M.; Li, K.; Lv, D.; Yang, X.; Gu, L.; Mao, N.; Feng, Q.; Xie, L.; et al. Exploring atomic defects in molybdenum disulfide monolayers. *Nat. Commun.* **2015**, *6*, 6293.
- (14) Li, H.-M.; Lee, D.-Y.; Choi, M. S.; Qu, D.; Liu, X.; Ra, C.-H.; Yoo, W. J. Metal-Semiconductor Barrier Modulation for High Photoresponse in Transition Metal Dichalcogenide Field Effect Transistors. *Sci. Rep.* **2014**, *4*, No. 4041.
- (15) Zhan, Y.; Liu, Z.; Najmaei, S.; Ajayan, P. M.; Lou, J. Large-Area Vapor-Phase Growth and Characterization of MoS₂ Atomic Layers on a SiO₂ Substrate. *Small* **2012**, *8*, 966–971.
- (16) Lan, C.; Li, C.; Yin, Y.; Liu, Y. Large-Area Synthesis of Monolayer WS₂ and Its Ambient-Sensitive Photo-Detecting Performance. *Nanoscale* **2015**, *7*, 5974–5980.
- (17) Plechinger, G.; Schrettenbrunner, F. X.; Eroms, J.; Weiss, D.; Schüller, C.; Korn, T. Low-Temperature Photoluminescence of Oxide-Covered Single-Layer MoS₂. *Phys. Status Solidi RRL* **2012**, *6*, 126–128.
- (18) Komsa, H.-P.; Kurasch, S.; Lehtinen, O.; Kaiser, U.; Krasheninnikov, A. V. From Point to Extended Defects in Two-Dimensional MoS₂: Evolution of Atomic Structure under Electron Irradiation. *Phys. Rev. B* **2013**, *88*, No. 035301.
- (19) Lin, J.; Cretu, O.; Zhou, W.; Suenaga, K.; Prasai, D.; Bolotin, K. I.; Cuong, N. T.; Otani, M.; Okada, S.; Lupini, A. R.; et al. Flexible Metallic Nanowires with Self-Adaptive Contacts to Semiconducting Transition-Metal Dichalcogenide Monolayers. *Nat. Nanotechnol.* **2014**, *9*, 436–442.
- (20) Ji, Q.; Zhang, Y.; Gao, T.; Zhang, Y.; Ma, D.; Liu, M.; Chen, Y.; Qiao, X.; Tan, P.-H.; Kan, M.; et al. Epitaxial Monolayer MoS₂ on Mica with Novel Photoluminescence. *Nano Lett.* **2013**, *13*, 3870–3877.
- (21) Choi, W.; Cho, M. Y.; Konar, A.; Lee, J. H.; Cha, G. B.; Hong, S. C.; Kim, S.; Kim, J.; Jena, D.; Joo, J.; et al. High-Detectivity Multilayer MoS₂ Phototransistors with Spectral Response from Ultraviolet to Infrared. *Adv. Mater.* **2012**, *24*, 5832–5836.
- (22) He, K.; Robertson, A. W.; Fan, Y.; Allen, C. S.; Lin, Y.; Suenaga, K.; Kirkland, A. I.; Warner, J. H. Temperature Dependence of the Reconstruction of Zigzag Edges in Graphene. *ACS Nano* **2015**, *9*, 4786–4795.
- (23) Kong, D.; Wang, H.; Cha, J. J.; Pasta, M.; Koski, K. J.; Yao, J.; Cui, Y. Synthesis of MoS₂ and MoSe₂ Films with Vertically Aligned Layers. *Nano Lett.* **2013**, *13*, 1341–1347.
- (24) Lee, Y.-H.; Zhang, X.-Q.; Zhang, W.; Chang, M.-T.; Lin, C.-T.; Chang, K.-D.; Yu, Y.-C.; Wang, J. T.-W.; Chang, C.-S.; Li, L.-J.; et al. Synthesis of Large-Area MoS₂ Atomic Layers with Chemical Vapor Deposition. *Adv. Mater.* **2012**, *24*, 2320–2325.
- (25) Wilson, J.; Yoffe, A. D. The Transition Metal Dichalcogenides Discussion and Interpretation of the Observed Optical, Electrical and Structural Properties. *Adv. Phys.* **1969**, *18*, 193–335.
- (26) He, J.; Hummer, K.; Franchini, C. Stacking effects on the electronic and optical properties of bilayer transition metal dichalcogenides MoS₂, MoSe₂, WS₂, and WSe₂. *Phys. Rev. B* **2014**, *89*, No. 075409.
- (27) Lee, J. U.; Kim, K.; Han, S.; Ryu, G. H.; Lee, Z.; Cheong, H. Raman signatures of polytypism in molybdenum disulfide. *ACS Nano* **2016**, *10*, 1948–1953.
- (28) Suzuki, R.; Sakano, M.; Zhang, Y. J.; Akashi, R.; Morikawa, D.; Harasawa, A.; Yaji, K.; Kuroda, K.; Miyamoto, K.; Okuda, T.; Ishizaka, K.; et al. Valley-dependent spin polarization in bulk MoS₂ with broken inversion symmetry. *Nat. Nanotechnol.* **2014**, *9*, 611–617.
- (29) Liu, L.; Qing, M.; Wang, Y.; Chen, S. Defects in Graphene: Generation, Healing, and Their Effects on the Properties of Graphene: A Review. *J. Mater. Sci. Technol.* **2015**, *31*, 599–606.
- (30) Robertson, A. W.; Lee, G. Do; He, K.; Yoon, E.; Kirkland, A. I.; Warner, J. H. The Role of the Bridging Atom in Stabilizing Odd Numbered Graphene Vacancies. *Nano Lett.* **2014**, *14*, 3972–3980.
- (31) Xie, F.; Lu, H.; Xiu, X.; Chen, D.; Han, P.; Zhang, R.; Zheng, Y. Low Dark Current and Internal Gain Mechanism of GaN MSM Photodetectors Fabricated on Bulk GaN Substrate. *Solid-State Electron.* **2011**, *57*, 39–42.
- (32) Avouris, P.; Freitag, M.; Perebeinos, V. Carbon-Nanotube Photonics and Optoelectronics. *Nat. Photonics* **2008**, *2*, 341–350.
- (33) Tsoukleri, G.; Parthenios, J.; Papagelis, K.; Jalil, R.; Ferrari, A. C.; Geim, A. K.; Novoselov, K. S.; Gallois, C. Subjecting a graphene monolayer to tension and compression. *Small* **2009**, *5*, 2397–2402.
- (34) Lee, C.; Wei, X.; Kysar, J. W.; Hone, J. Measurement of the elastic properties and intrinsic strength of monolayer graphene. *Science* **2008**, *321*, 385–388.
- (35) Park, S. D.; Lee, S. W.; Kang, S.; Bang, I. C.; Kim, J. H.; Shin, H. S.; Lee, D. W.; Lee, D. W. Effects of nanofluids containing graphene/graphene-oxide nanosheets on critical heat flux. *Appl. Phys. Lett.* **2010**, *97*, No. 023103.
- (36) Popov, A. M.; Lebedeva, I. V.; Knizhnik, A. A.; Lozovik, Y. E.; Potapkin, B. V. Commensurate-incommensurate phase transition in bilayer graphene. *Phys. Rev. B* **2011**, *84*, No. 045404.
- (37) Kresse, G.; Furthmüller, J. Efficient Iterative Schemes for Ab Initio Total-Energy Calculations Using a Plane-Wave Basis Set. *Phys. Rev. B* **1996**, *54*, 11169–11186.

- (38) Blöchl, P. E. Projector Augmented-Wave Method. *Phys. Rev. B: Condens. Matter Mater. Phys.* **1994**, *50*, 17953–17979.
- (39) Perdew, J. P.; Burke, K.; Ernzerhof, M. Generalized Gradient Approximation Made Simple. *Phys. Rev. Lett.* **1996**, *77*, 3865–3868.
- (40) Grimme, S. Semiempirical GGA-Type Density Functional Constructed with a Long-Range Dispersion Correction. *J. Comput. Chem.* **2006**, *27*, 1787–1799.
- (41) Monkhorst, H. J.; Pack, J. D. Special Points for Brillouin-Zone Integrations. *Phys. Rev. B* **1976**, *13*, 5188–5192.